CrossMark
click for updates

Synthesis and exceptional thermal stability of Mg-based bimetallic nanoparticles during hydrogenation†

Gopi Krishnan,[*a] Raluca F. Negrea,[b] Corneliu Ghica,[b] Gert H. ten Brink,[a] Bart J. Kooi[a] and George Palasantzas[a]

Here we report the extraordinary thermal stability of Mg rich bimetallic nanoparticles (NPs), which is important for hydrogen storage technology. The enhanced NP stability is accomplished because of two critical improvements: (i) no void development within NPs (nanoscale Kirkendall effect) during their formation and (ii) suppressed Mg evaporation and NP hollowing during Mg hydrogenation at elevated temperature. The mechanism leading to the improved thermal stability of Mg-based bimetallic NPs is shown to be due to MgH_2 hydride formation before evaporation can take place. These findings were tested for various compositions of Mg with Ni, Cu, and Ti, which are interesting combinations of materials for hydrogen storage systems. To achieve this we first demonstrate the synthesis mechanism of Mg–Ni and Mg–Cu NPs, which is well controlled at the single particle level, in order to accomplish multi-shell, alloy and intermetallic structures of interest for hydrogen storage tests. Aberration corrected transmission electron microscopy was carried out to unravel the detailed atomic structure and composition of the bimetallic NPs after production, processing, and hydrogenation. Finally, a simple and effective methodology is proposed for tuning the composition of the Mg-based bimetallic NPs based on the temperature-dependent nucleation behavior of NPs in the gas-phase.

Introduction

Magnesium (Mg) with its light weight and 7.6 wt% of H storage capacity is considered as one of the potential candidates for hydrogen storage.[1] The slow kinetics for hydrogen absorption/desorption and the high thermodynamic stability arising from the negative (low) enthalpy of MgH_2 formation have been the motivation behind the considerable attention that is paid to Mg nanoparticles (NPs). Although the decrease in Mg NP size (<2 nm) is considered as a favorable forward step towards reducing the formation enthalpy of MgH_2,[2] the size reduction below 20 nm turned out to have formidable consequences for Mg NPs. For example in ref. 3–5 it was found that the high vapor pressure of smaller Mg NPs (<20 nm) leads to higher evaporation rates of Mg than that for larger NPs (>20 nm), where they evaporate much faster during hydrogenation at temperatures above room temperature. In ref. 5 it was demonstrated that void

formation occurs for NPs larger than 10 nm, and that hollow MgO NPs are formed for NPs less than 10 nm due to the oxidation induced nanoscale Kirkendall effect during NP production.[3] The latter is the result of faster outward diffusion of Mg ions with simultaneous inward diffusion of vacancies to compensate for the unequal material flow due to the different atomic diffusivities. Furthermore, the vacancies supersaturate to form voids within the NPs. As a result smaller Mg NPs (<10 nm) completely transform into hollow NPs, and the larger NPs (>10 nm) develop voids in the vicinity of their facets within the nanoparticles and these voids grow further during hydrogenation.[3] Although these phenomena present formidable barriers for the successful implementation of Mg NPs in hydrogen storage, the use of Mg bimetallic NPs might alleviate the issues above.

Indeed, bimetallic NPs are considered as an interesting class of materials, where the chemical and physical properties can be tailored based on composition, size, and atomic ordering. In fact, Mg-based bimetallic NPs produced to date are mostly based on bottom up methods consisting of inert-gas condensation,[6] spark discharge generation,[7] and the hydrogen plasma–metal reaction/arc method.[8,9] However, none of these methods have shown a well-controlled tuning of sizes, structural motifs, and composition of bimetallic NPs. In addition, although the gas-phase synthesis of NPs via DC-magnetron sputtering is well known to produce metallic and bimetallic NPs, only recently the

[a]Zernike Institute for Advanced Materials and the Materials Innovation Institute, University of Groningen, Nijenborgh 4, 9747 AG Groningen, The Netherlands. E-mail: gopi.k.krish@gmail.com

[b]National Institute for Materials Physics, P.O. Box MG-7, Magurele, Ilfov, RO 77125, Romania

capability of this technique to control different bimetallic structures was demonstrated.[10,11] In fact, we demonstrated a general methodology to tune various structures of, bulk immiscible, bimetallic NPs at the single particle level using our home modified Mantis nanocluster source.[10]

Bimetallic Mg-rich based NPs combined with other metals like Ni, Cu and Ti, which are interesting as hydrogen storage materials,[1] are highly challenging to synthesize using gas-phase synthesis with a controlled composition and structure. This can be attributed to the different physical properties (*e.g.* vapor pressure and melting point) of Mg and the combined elements (*e.g.* Ni, Cu and Ti), which affect the size, nucleation, and composition of the bimetallic NPs. These factors demand change of sputtering target composition in order to alter the NP chemical composition. Here, however, we will demonstrate that it is feasible to achieve composition tuning of Mg–Ni, Mg–Cu, and Mg–Ti NPs based on a temperature dependent nucleation behavior of Mg, Ni, and Cu using only a single composition (sectioned) material target for magnetron sputtering and gas phase synthesis of NPs. To the best of our knowledge, tuning different structures of Mg-based bimetallic NPs, tailoring composition during production, and thermal stability have not been reported before.

Hence in this article we demonstrate: (i) the complete suppression of voids during the synthesis of Mg–Ni, Mg–Cu, and Mg–Ti NPs with Mg rich composition, (ii) the improved thermal stability of Mg–(Ni, Cu, Ti) without the formation of a hollow Mg core during hydrogenation of NPs at 250 °C and 10 bar pressure of H_2, and (iii) a synthesis methodology to tailor the composition and different structures of Mg-based bimetallic NPs at a single particle level, where proof for the different structures comes from aberration corrected transmission electron microscopy. Finally this paper is dedicated only to the synthesis and in depth characterization of Mg based bimetallic nanoparticles, as well as their thermal stability during hydrogenation.

Experimental methods

Synthesis

The Mg–Ni, Mg–Cu and Mg–Ti bimetallic nanoparticles with various structures (alloys, multishell and multiphase) and compositions were produced by using a home modified nanoparticle system Nanosys500 from Mantis Deposition Ltd. (http://www.mantisdeposition.com). The sample chamber was evacuated to a base pressure of $\sim 1 \times 10^{-8}$ mbar with an oxygen partial pressure of $\sim 10^{-11}$ mbar. Supersaturated metal vapor is produced by magnetron sputtering of a sectioned target shown (99.95% purity of Mg, Ni, Cu and Ti as obtained from Alpha Aesar) in Fig. 1(a) or (b) in an inert argon atmosphere (pressure of $\sim$0.25 mbar with an appropriate discharge current depending on the choice of the structures that were synthesized). The supersaturated metal vapor is then cooled by argon gas in order to form nuclei, which can subsequently grow into nanoparticles. The nanoparticles formed in the aggregation volume are removed fast by the use of argon which act as a drift and sputter gas. The tuning of the thermal environment and energy

was made by varying the discharge current and by keeping the pressure constant inside the aggregation volume.

TEM analysis

The nanoparticles transported from the aggregation volume were deposited onto 25 nm thick silicon-nitride membranes, which were used for Transmission Electron Microscopy (TEM) analysis using a JEOL 2010F and JEOL ARM 200F aberration corrected TEM. The TEM investigations performed on a JEM ARM 200F electron microscope is provided with a probe Cs corrector and a Quantum SE Gatan Image Filter. The microscope was operated at 200 kV acceleration voltage. For the EELS spectral images we used a convergence semiangle of 20 mrad and a collection semiangle of 49 mrad for a camera length of 3 cm. In order to create a composition line profile across the nanoparticles, an EEL spectrum has been extracted from each pixel along the diameter of the nanoparticle. Each extracted spectrum has been quantified using the Hartree–Slater model for the differential cross-section calculation and the power-law for the background model.

Results and discussion

Fig. 1(a) and (b) show bright-field TEM images of Mg–Ni nanoparticles before and after hydrogenation. The NPs show no void formation during their production and no Mg evaporation after hydrogenation at 250 °C (under 10 bar H_2 pressure for 72 h). Therefore the present bimetallic NPs show a greatly improved thermal stability as compared to monometallic Mg NPs.[3] The compositions of the Mg-rich NPs were 80 ± 3 at% Mg and 20 ± 3 at% Ni (measured using STEM-EELS analysis) with the as-prepared NP structure being solid solution. Our previous analysis has proven that Mg NPs can evaporate and form hollow Mg very rapidly at this temperature and H_2 pressure.[3] Moreover, also bimetallic Mg–Cu and Mg–Ti NPs with similar compositions were tested for improved stability, as shown in the bright-field TEM images of Fig. 1(d, e, g and h).

Although the MgH_2 formation can be achieved at lower H_2 pressure and time, our motivation for prolonged exposure is to observe their long term thermal stability in comparison with monometallic Mg NPs. The diffraction patterns of Fig. 1(c), (f) and (i) confirm that the corresponding NPs are fully hydrogenated having an α-MgH_2 rutile phase (see the HRTEM image in Fig. 3(b) in the ESI†). After hydrogenation, Mg–Ni and Mg–Cu NPs show segregation and phase separation of Ni and Cu to the center of (most of) the NPs that are shown in Fig. 1 (compare (b) with (a) and (e) with (d)). This segregation phenomenon can be attributed to the following systematic reasons: (1) lower enthalpy of MgH_2 formation (-37 kJ mol^{-1} H), as compared to Ni (4.5 kJ mol^{-1} H) and Cu (24 kJ mol^{-1} H), which acts as a driving force for segregation; (2) enhanced atomic mobility of atoms under the influence of absorbed hydrogen in the NPs, as observed in bulk materials;[12–14] (3) surface energy difference between MgH_2 and Ni (or Cu) drives Mg atoms to the surface to form an MgH_2 shell, and simultaneously Ni (or Cu) atoms are
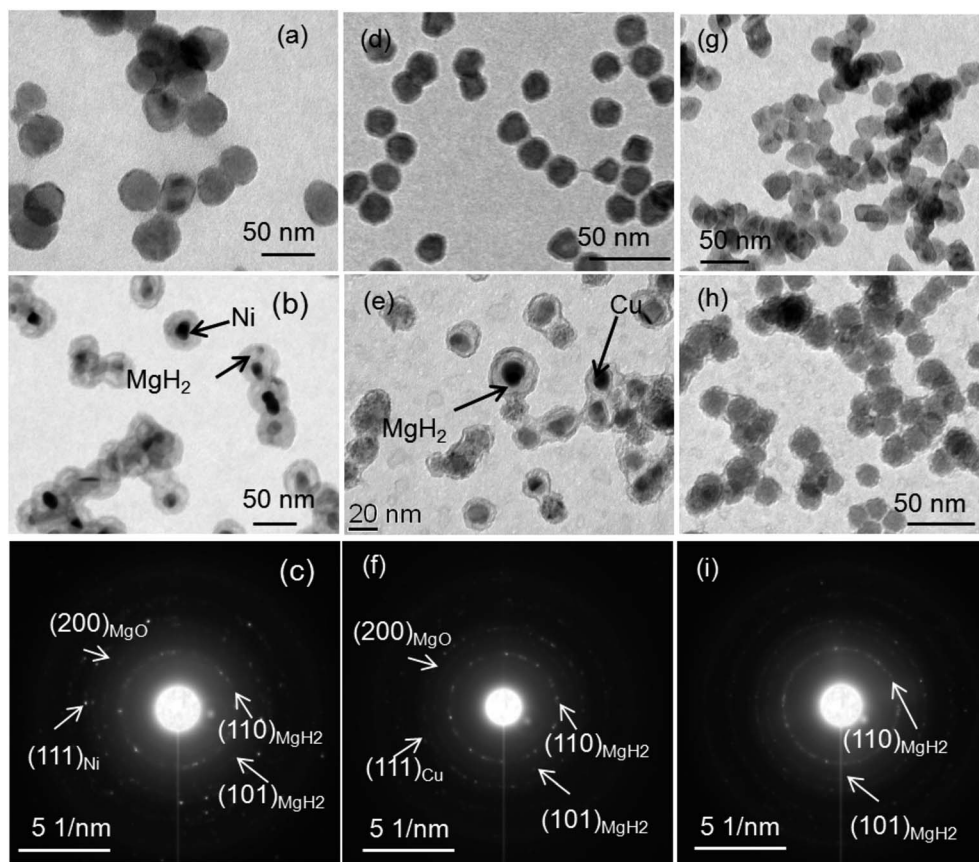
Fig. 1 TEM results of Mg–Ni (a–c), Mg–Cu (d–f) and Mg–Ti (g–i) NPs before and after hydrogenation without void formation. (a, d and g) Bright-field TEM images of Mg–Ni NPs with 80 ± 3 at% of Mg, Mg–Cu NPs with 81 ± 3 at% of Mg and Mg–Ti NPs with 85 ± 4 at% of Mg before hydrogenation. (b, e and h) Bright field TEM images of Mg–Ni, Mg–Cu and Mg–Ti NPs after hydrogenation at 250 °C and 10 bar H_2. Mg–Ni and Mg–Cu NPs exhibit phase separation of Ni and Cu (center), and MgH_2 on the outer shell. The Mg–Ti NPs do not show any phase separation. (c, f and i) Diffraction patterns of the Mg–Ni, Mg–Cu and Mg–Ti NPs after hydrogenation with a clear indication of the rutile MgH_2 formation in all cases.

pushed to the center where they finally form a Ni (or Cu) core (see the HAADF-STEM image in Fig. 3(a) in the ESI†).

Our initial observations indicate that phase separation does not take place when Mg–Ni NPs are annealed at 250 °C in a vacuum, indicating the clear influence of hydrogen on phase separation. In contrast, phase separation upon hydrogenation (as observed for Mg–Ni and Mg–Cu NPs) does not occur for Mg–Ti NPs indicating their unique behavior as it is shown in Fig. 1(h). However, the lower enthalpy of TiH_2 formation (-72 kJ mol^{-1} H) as compared to MgH_2 (-37 kJ mol^{-1} H) indicates that hydrogen should in general still favor phase separation. Moreover, in the case of Mg–Ti thin films phase separation was not observed also after hydrogenation at low temperature and pressure.[15,16] The coherent structure and equal molar volume of TiH_2, Mg and influence of hydrogen on the stabilization of Mg–Ti alloys by reducing the enthalpy of formation from positive to negative (Mg and Ti are immiscible systems with a positive enthalpy of formation) are two reasons considered to inhibit phase segregation in thin films.[15,16] Nevertheless, a full understanding is still missing. Our detailed study to improve the understanding of this behavior for Mg–Ti NPs will be reported elsewhere. In any case enhanced thermal stability of

bimetallic Mg NPs is preserved for an Mg concentration of less than <85 at%, which is valid for Ni, Cu and Ti. Above this Mg concentration void formation and voiding of Mg cores slowly start to develop during synthesis and hydrogenation depending on the NP size where it is of course more pronounced for smaller NPs (see Fig. 4 in the ESI†).

The suppression of void formation in Mg-based bimetallic NPs during their production can be explained qualitatively by three important factors: (1) the presence of Ni, Cu and Ti at the interface of the metal/metal-oxide (Mg/MgO) suppresses vacancy supersaturation and thereby blocks the coalescence of vacancies to form voids or reduces initial nucleating sites for void formation and subsequent growth; (2) the presence of vacancy sinks in bimetallic Mg NPs near the metal/metal-oxide interface for vacancy annihilation; (3) outward diffusion of Mg becomes slow during the process of hydrogenation by the formation of intermetallic/alloy near the interface. Indeed, a similar kind of strategy has been employed in thin films of two metals separated with an intermediate alloy layer (made of a combination of the same metals), which efficiently inhibits the void formation due to their reduced atomic diffusivity.[17,18]

More important is the fact that the Mg-based bimetallic NPs also show an increased thermal stability during hydrogenation as compared to pure Mg nanoparticles. This can be attributed to the solid solution (alloy) structure of Mg-based bimetallic NPs, which significantly lowers the Mg vapor pressure as compared to monometallic NPs. The latter can be understood by the fact that the added metals (Ni, Cu, and Ti) have higher melting and boiling points than Mg (in general high boiling point metals have low vapor pressure). For example, Ni has (compared to Mg) low vapor pressure and high thermal stability at all relevant temperatures. Therefore, Mg-based bimetallic NPs with an alloy structure should show better thermal stability than Mg. This is confirmed here for Mg–Ni, Mg–Cu and Mg–Ti bimetallic NPs with Mg-rich composition.

During hydrogenation the segregation and phase separation do not lead to void formation within NPs. This can be the effect of stable MgH_2 formation during phase separation of Ni, as MgH_2 is thermally more stable than Mg, which prevents hollowing of Mg and increases the thermal stability of NPs. In the case of monometallic Mg NPs we observed that the Mg evaporation takes place rapidly before the formation of the MgH_2 phase occurs due to their high vapor pressure. Therefore, in the case of Mg-based bimetallic NPs the enhanced stability arises from: (a) the lower vapor pressure of Mg due to the alloy structure, which retards the Mg evaporation, and (b) subsequently allowed the formation of MgH_2, which further clearly enhances the thermal stability of the Mg-based NPs.

To support this claim we demonstrate that Mg–Ni NPs, with an initial multi-shell structure as shown in Fig. 3(a), when they undergo hydrogenation under two different conditions (250 °C at 10 bar H_2, and 150 °C at 5 bar H_2) give two different outcomes. First, the Mg–Ni NPs at 250 °C and 10 bar H_2 show phase separation, similar to that observed in Fig. 1(a), while in the second case, at 150 °C and 5 bar H_2, the NPs do not show any phase separation and MgH_2 formation. Moreover, the latter NPs only show the presence of an MgO shell and complete absence of Mg in the core of the NP. Ni of course remains, which also suggests that when Mg is not hydrided sufficiently fast it can still easily evaporate (Fig. 5 in the ESI†).

In order to be able to control this void formation (nanoscale Kirkendall effect) and thermal stability of Mg rich bimetallic NPs we have developed a synthesis methodology to tune the composition and structure of the Mg-based bimetallic NPs, where for Mg–Ni and Mg–Cu three categories can be distinguished: multi-shell/onion structures, intermetallic compounds, and (solid-solution) alloy structures. The nucleation and growth of the bimetallic NPs were controlled via regulation of the discharge current applied to the material target for DC magnetron sputtering, which is one of the possible paths to control the NP structures formed during high pressure gas-phase condensation.[10,19] Indeed, regulation of the discharge current gives a direct control over the thermal environment the NPs experience during their formation, since it allows tuning of the density of the plasma and thus the energy of the sputtering Ar ions and growing NPs. As a result, this process allows tuning of different temperature regimes (as the discharge current increases the plasma temperature also increases under constant gas flow conditions) and cooling rates for the NPs during their formation.[10] The temperature/thermal environment affects strongly the NP nuclei formation, and their nucleation rate, which is strongly element specific at different discharge currents. Effectively we can thus use this dependence to tune the structure and composition of the bimetallic NPs.

In general during binary element thin film formation the elements with high vapor pressure (under the synthesis conditions) will share higher percentages of the composition in the final structure. However, in bimetallic NPs, e.g. Mg–Ni, the high vapor pressure element (Mg) does not dominate the final composition of the NPs but rather it depends on the rate of nuclei formation of Ni (high melting point element) and subsequent growth (and intermixing) of both Mg and Ni. This is especially valid when the combined elements have large differences in their physical properties (e.g. vapor pressure and melting points). From our previous observations, a metal with higher melting point (higher solidification temperature) will always tend to be enriched in the NPs compared to the accompanying metal in the binary system.[10] Fig. 2(a) shows a schematic of the bimetallic NP formation at different discharge currents at a constant flow rate, while Fig. 2(b) shows a schematic of the temperature profile the NPs experience at different discharge currents.

Furthermore, Fig. 3(a) shows a bright-field TEM image of Mg–Ni nanoparticles synthesized at 0.250 A discharge current showing a multi-shell structure (i.e. as opposed to the alloy structure shown in Fig. 1(a)), which can be confirmed from the observed variations in contrast. Fig. 3(c) shows a STEM-EELS
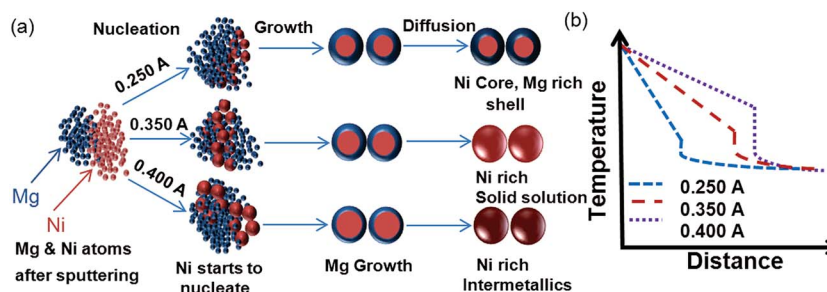

Fig. 2 (a) Schematic illustration of the Mg-based bimetallic NP formation at various discharge currents. (b) Effect of discharge current on the temperature profile and cooling rate of the NPs.
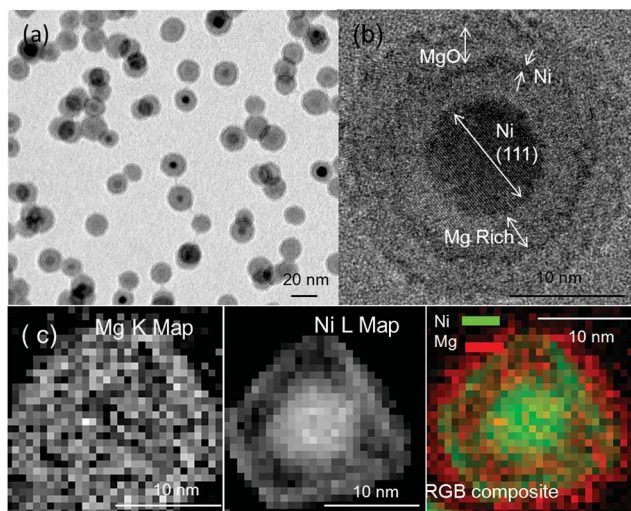
Fig. 3 Bright-field TEM images of the Mg–Ni NPs produced at 0.250 A discharge current. (b) HRTEM image of the Mg–Ni NP showing a Ni core in which the (111) planes are resolved. (c) STEM-EELS mapping of the Mg–Ni NP.

spectral mapping of a corresponding NP, which reveals the multi-shell structure. The NP shows a Ni-core with towards the outside a sequence of Mg rich/Ni/MgO shells as indicated in the figure, where particularly the intermediate Ni shell is relatively thin. Fig. 3(b) shows a HRTEM image of the NPs indicating the Ni (111) lattice planes, which confirms the presence of Ni as a core. To understand more in detail the composition of Mg and Ni, we present in Fig. 4(a) and (b) a line profile of the NP

composition from the STEM-EELS spectrum. The composition distribution in a single NP can be clearly seen along with the Ni and Mg rich regions confirming the presence of the multi-shell structure.

In order to understand this multi-shell structure formation, we schematically illustrate this process for Mg–Ni NPs in Fig. 4(c), and show how oxidation plays a central role. Unlike most other metals, Mg NPs form an oxide shell during their production, even in ultra-high vacuum systems, due to the very high affinity of Mg for oxygen.[5] As shown in Fig. 4(c), the particle produced initially will have a core–shell structure with Ni as a core, and an Mg-rich region as a shell. During oxidation Mg atoms diffuse into the surface while the Ni atoms in the Mg-rich shell are pushed backwards as Mg has higher affinity for oxygen to form MgO ($\Delta H = -601$ kJ mol^{-1}) rather than Ni to form NiO ($\Delta H = -239$ kJ mol^{-1}). Moreover, the surface energy of MgO is lower than Ni, $\gamma_{MgO} < \gamma_{Mg} < \gamma_{Ni}$, which also favors MgO to be an outer shell. Finally this leads to an outer MgO shell followed by a subsurface Ni shell. This process stops once Mg forms an MgO oxide of certain thickness because the electron transfer (tunneling) mechanism from the metal-oxide interface to the outer oxide surface, necessary for oxidation to occur, decreases exponentially at room temperature when the thickness of the oxide shell increases linearly.[5,20,21] Remarkably, this process thus enables the formation of a multi-shell structure within a single NP.

Fig. 5(a) shows a bright field TEM image of the Mg–Ni NP produced with a higher discharge current of 0.400 A, and Fig. 5(b) shows a corresponding HRTEM image demonstrating the presence of the intermetallic MgNi$_2$ compound (in a mixed
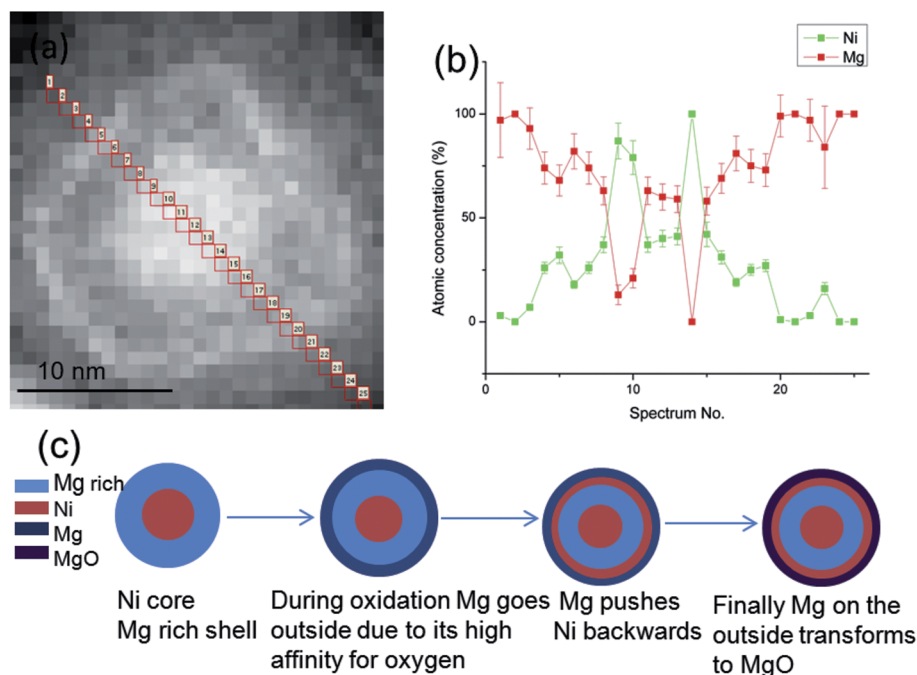

Fig. 4 (a) HAADF-STEM image of an Mg–Ni NP. (b) Composition line profile of the Mg–Ni NP from STEM-EELS, from spectra 1 to 25 as shown in (a) in red. (c) Schematic illustration of the multi-shell structure formation during oxidation of Mg–Ni NPs synthesized at 0.250 A discharge current.
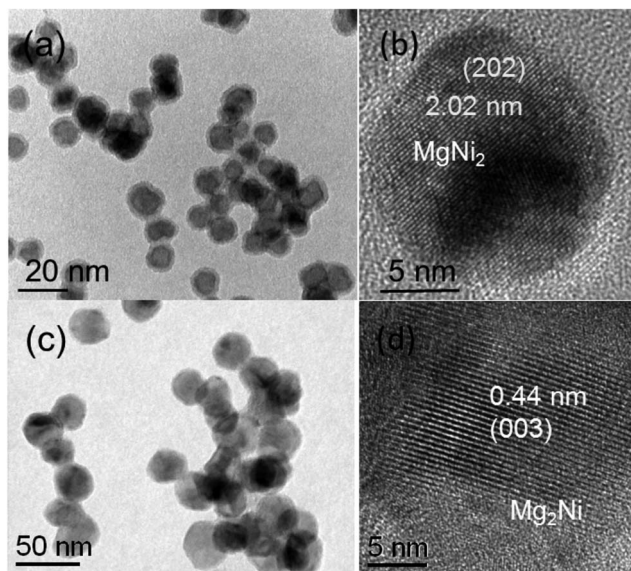
Fig. 5 (a) Bright-field TEM image of the Mg–Ni NPs produced at 0.400 A (1/2Mg + 1/2Ni section targets). (b) HRTEM image of the intermetallic $MgNi_2$ structure. (c) Bright-field TEM image of the Mg–Ni NP produced at 0.350 A discharge current with 3/4Mg + 1/4Ni section targets. (d) HRTEM image of the intermetallic Mg_2Ni.

state) with a clearly increased Ni at.% than that produced in Fig. 3 (∼73 versus ∼42 at% Ni). Similarly, an intermediate current 0.350 A also shows a solid solution in the Mg–Ni NPs but with a Ni concentration at an intermediate level (∼60 at% Ni) between those obtained with 0.250 and 0.400 A discharge currents. The latter confirms the fact that at higher discharge current the temperature profile that these NPs undergo is in general higher allowing the formation of a solid solution/ intermetallic structure more enriched in the higher melting point element. However, for hydrogen storage applications we need Mg-rich particles as the increase in Ni concentration would not only increase the overall weight of the material but also simultaneously reduce the hydrogen storage capacity. Therefore, instead of using half section targets of Mg and Ni, we adopted a section target of 3/4 Mg and 1/4 Ni. As a result the Mg–Ni NPs produced at 0.250 A show an increased Mg concentration of 80 at% in solid solution, which is in fact the result shown in Fig. 1(a)–(c). With a discharge current of 0.350 A an intermetallic Mg_2Ni compound is formed consisting of 70 at% Mg as shown in Fig. 5(c) and (d). The latter results again confirm the fact that at higher discharge current the (high vapor pressure) Mg concentration reduces against that of the high melting point element Ni.

In order to see now the evolution of Mg–Cu NPs with a similar strategy as for the Mg–Ni system, we selected a section target of 1/2 Mg and 1/2 Cu. Fig. 6(a) shows a HAADF-STEM image and Fig. 6(b) shows a bright field TEM image of the Mg–Cu NPs produced at 0.250 A. In comparison with Mg–Ni under the same conditions, the Mg–Cu NPs also display a similar kind of structure. However, a detailed compositional line profile analysis of the NPs from STEM-EELS shows a variation of the Cu composition from the center to the outer surface of the NP as it

is shown in Fig. 6(c) and (d). These profiles clearly show, unlike Ni, that Cu does not have a pure core and a multiple shell structure but it rather forms a multiphase region from the center to the outer surface of the particles. The Mg–Cu NP structure consists of a core region, which is a solid solution rich in Cu as it is verified from HRTEM and HRSTEM images (see Fig. 6 in the ESI†). This is followed by an Mg rich solid solution region, a very thin Cu shell, and an MgO shell at the outer surface. Similar to the Ni case, Cu is also present at the subsurface as a shell before the MgO layer, as it can be seen in HAADF-STEM images of Fig. 6(a). Once the discharge current is increased further to 0.350, it forms an Mg_2Cu intermetallic. This is shown in Fig. 6(e) and the corresponding HRTEM image of Fig. 6(f), which displays the lattice spacing of the Mg_2Cu (040) planes. Finally, as the discharge current is increased further to 0.400 A, the NPs form a solid solution, Fig. 6(g), with compared to Mg_2Cu a further increase in Cu concentration.

If we compare now the Ni and Cu concentrations in Mg–Ni and Mg–Cu NPs produced under the same conditions, Fig. 6(h), it is evident that the Ni concentration is more than twice the one of Cu. When the discharge current is increased the increase in concentration of Ni is also more pronounced than that of Cu. This can be attributed to the differences in the rate of nuclei formation and their growth under that particular condition. To understand the formation of Mg–Ni and Mg–Cu NPs we have to understand the solidification of Mg–Ni and Mg–Cu. From the Mg–Ni equilibrium phase diagram, Ni will solidify first because it has a higher melting point of 1455 °C as compared to that of Mg of 650 °C. In an atomic vapor of Mg–Ni, Ni will solidify first and form nuclei and then Mg will start to solidify on Ni, because it is relatively easy for Mg to grow on Ni. This is also supported by our experimental observation that we do not see any separate pure Mg and Ni NPs. According to our previous observation on Mg NPs, Mg always tends to have a difficulty in homogenous nucleation, and it would require some species of impurity to nucleate. At 0.250 A discharge current (plasma temperature (T_p) = 2.0×10^6 K), Mg is able to grow relatively easy, as the thermal environment and gas temperature are relatively moderate and thus favorable for Mg growth. As the discharge current is increased further to 0.350 A ($T_p = 2.6 \times 10^6$ K) or 0.400 A ($T_p = 3.0 \times 10^6$ K) (at constant gas flow), the temperature of the plasma is increased and the thermal environment the NPs experience is also changed favoring the formation of single alloy/solid solution NPs. Since Mg has relatively low solidification temperature it is not able to grow as easy in the 0.400 A plasma as it was in the 0.250 A one. These differences in nucleation and growth conditions for increasing discharge current thus favor a Ni-rich composition.

In the case of Mg–Cu, Cu solidifies and forms nuclei first and afterwards Mg grows on them, but the main difference with Ni is that Cu has (1) a clearly lower melting point than that of Ni (1085 °C versus 1455 °C) and thus nucleates at temperatures more close to the solidification temperature of Mg (650 °C) and (2) still better atomic mobility under these conditions than Ni and forms multi-phase structures instead of a multi-shell structure that is observed in Mg–Ni NPs. Note that the phase diagram of both Mg–Cu and Mg–Ni is rather similar. Similar to
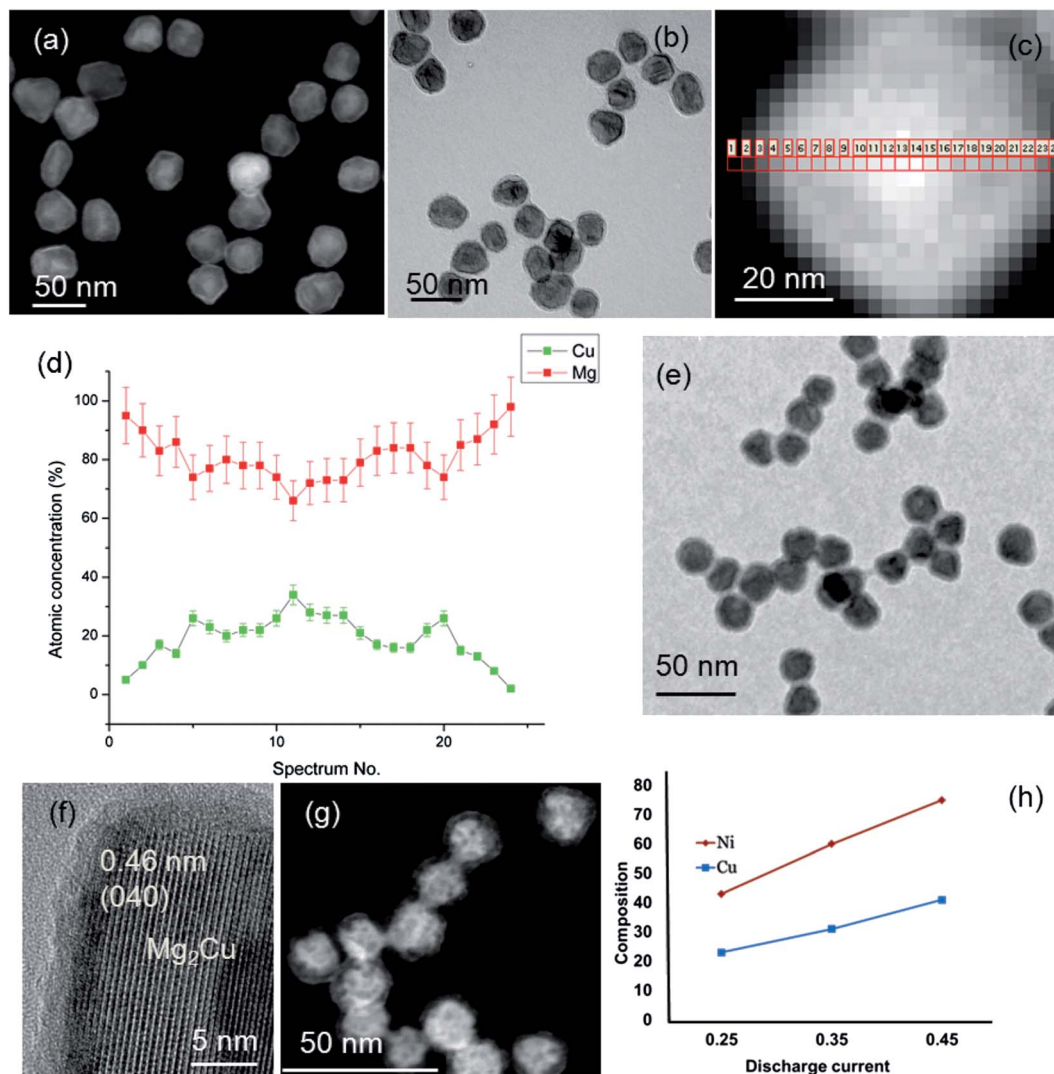
Fig. 6   (a) HAADF-STEM image of the Mg–Cu NPs synthesized at 0.250 A. (b) Bright field TEM image of the same Mg–Cu NPs. (c) HAADF-STEM image of an NP synthesized at 0.250 A discharge current, whose composition line profile is shown in (d). (d) Composition line profile of the NP from spectra 1 to 24 as shown in (c). (e) Bright field TEM image of the Mg–Cu NPs synthesized at 0.350 A with an intermetallic Mg$_2$Cu structure. (f) HRTEM image of the intermetallic Mg$_2$Cu structure. (g) HAADF-STEM image of Mg–Cu NPs synthesized at 0.400 A with a solid solution (alloy) structure, where the Cu composition is higher than that of the Mg–Cu NPs shown in (a) and (e). (h) Variation of Ni and Cu concentrations in the Mg–Ni and Mg–Cu NPs produced at different discharge currents for 1/2Mg + 1/2Ni section targets.

Mg–Ni, Mg–Cu also forms single alloy/solid solution structured NPs at 0.350 and 0.400 A discharge currents, however the Cu concentrations in the NPs are observed clearly lower than the Ni ones (and the Mg concentrations thus higher, *cf.* Fig. 6(h)). This can be attributed to the lower melting point temperature difference between Cu and Mg than between Ni and Mg. Similar behavior is also observed in the case of Mo–Cu, which has higher Mo concentration than Cu at a high discharge current of 0.550 A (Mo has a melting point of 2623 °C).[10] In addition, the NPs produced from a 3/4Mg–1/4Cu section target show a lower concentration of Cu as compared to that of Ni, produced under exactly the same conditions, as it is shown in Fig. 5(c).

At higher discharge current, the cooling process is effectively reduced due to high temperature (kinetic energy) of the Ar gas molecules that act as a source for energy drain and nuclei

formation. Since Cu has a high-energy transfer function and lower bond energy, its nucleation rate is diminished yielding a reduced Cu concentration within NPs.[10] In the case of Mg–Ti we also observe the concentration of Ti to increase at higher discharge current, *i.e.* similar behavior as observed for Ni and Cu in Mg–Ni and Mg–Cu. However, we do not observe a multi-shell or multiphase structure as in Mg–Ni and Mg–Cu, which reveals the important point that Mg is not able to dissolve in Ti at 0.250 A discharge current (Mg and Ti are immiscible) and pure Mg develops on top of a pure Ti core during NP formation. As a result no Ti subsurface shell is observed (see Fig. 7 in the ESI†). This also proves the oxidation mechanism of Mg–Ni and Mg–Cu produced at 0.250 A discharge current, where subsur-face Ni and Cu are accumulated due to the displacement of Ni and Cu backwards within the NP. In Mg–Ti it is always pure Mg

that surrounds Ti (no Mg rich area is present), which then logically implies that during oxidation subsurface Ti cannot develop.

Conclusions

We have demonstrated the synthesis of bimetallic Mg-based NPs (Mg–Ni, Mg–Cu, and Mg–Ti) with exceptional thermal stability during both their production and hydrogenation, where no void formation takes place. This exceptional thermal stability arises from (1) the addition of high melting point metals (Ni, Cu, and Ti) to Mg in a kind of solid solution and (2) the formation of hydride MgH$_2$ before Mg evaporates. This stability is maintained for high Mg concentrations in the NPs up to 85 at%. We also demonstrated a synthesis methodology for tuning the structure and composition of Mg-based bimetallic NPs, which are of interest for high capacity hydrogen storage systems with enhanced surface to volume ratio architectures. Proof for the different NP structures synthesized has been provided by aberration-corrected TEM at the atomic and nanoscale level.

Acknowledgements

References

1 L. Schlapbach and A. Züttel, *Nature*, 2001, **414**, 353.
2 R. W. P. Wagemans, J. H. van Lenthe, P. E. de Jongh, A. J. van Dillen and K. P. de Jong, *J. Am. Chem. Soc.*, 2005, **127**, 16675.
3 G. Krishnan, B. J. Kooi, G. Palasantzas, Y. Pivak and B. Dam, *J. Appl. Phys.*, 2010, **107**, 052504.
4 G. Krishnan, G. Palasantzas and B. J. Kooi, *Appl. Phys. Lett.*, 2010, **97**, 261912.
5 B. J. Kooi, G. Palasantzas and J. T. M. De Hosson, *Appl. Phys. Lett.*, 2006, **89**, 161914.
6 E. Callini, L. Pasquini, L. H. Rude, T. K. Nielsen, T. R. Jensen and E. Bonetti, *J. Appl. Phys.*, 2010, **108**, 073513.
7 A. Anastasopol, T. V. Pfeiffer, J. Middelkoop, U. Lafont, R. Canales-Perez, A. Schmidt-Ott, F. M. Mulder and S. W. H. Eijt, *J. Am. Chem. Soc.*, 2013, **135**, 7891.
8 J. P. Lei, H. Huang, X. L. Dong, J. P. Sun, B. Lu, M. K. Lei, Q. Wang, C. Dong and G. Z. Cao, *Int. J. Hydrogen Energy*, 2009, **34**, 8127.
9 H. Shao, H. Xu, Y. Wang and X. Li, *Nanotechnology*, 2004, **15**, 269.
10 G. Krishnan, M. A. Verheijen, G. H. ten Brink, G. Palasantzas and B. J. Kooi, *Nanoscale*, 2013, **5**, 5375.
11 Y. Xu and J. Wang, *Adv. Mater.*, 2008, **20**, 994.
12 K. Watanabe, N. Ōkuma, Y. Fukai, Y. Sakamoto and Y. Hayashi, *Scr. Mater.*, 1996, **34**, 551.
13 H. Noh, J. D. Clewley, T. B. Flanagan and A. P. Craft, *J. Alloys Compd.*, 1996, **240**, 235.
14 B. Rodmacq, M. Maret, J. Laugier, L. Billard and A. Chamberod, *Phys. Rev. B: Condens. Matter Mater. Phys.*, 1988, **38**, 1105.
15 D. M. Borsa, R. Gremaud, A. Baldi, H. Schreuders, J. H. Rector, B. J. Kooi, P. Vermeulen, P. H. L. Notten, B. Dam and R. Griessen, *Phys. Rev. B: Condens. Matter Mater. Phys.*, 2007, **75**, 205408.
16 I. J. T. Jensen, S. Diplas and O. M. Løvvik, *Appl. Phys. Lett.*, 2012, **100**, 111902.
17 J. C. Fletcher, F. G. Arcella, G. G. Lessmann, R. A. Lindberg, Bimetallic junctions, *U.S. pat.* 4033504, 1977.
18 H. Lutz and O. Pous, *Hydrogen Met., Proc. Int. Congr., 2nd*, 1977, **2**, 1F5.
19 J. Qiu and J. Wang, *Adv. Mater.*, 2007, **19**, 1703.
20 A. T. Fromhold and E. L. Cook, *Phys. Rev.*, 1967, **163**, 650.
21 A. T. Fromhold and E. L. Cook, *Phys. Rev.*, 1967, **158**, 600.